

Article

Numerical Modeling of 3D Chiral Metasurfaces for Sensing Applications

Alexa Guglielmelli ^{1,2,†} , Giuseppe Nicoletta ^{1,2,†} , Liliana Valente ¹, Giovanna Palermo ^{1,2,*} 
and Giuseppe Strangi ^{1,2,3}

¹ NLHT-Lab, Department of Physics, University of Calabria, via Ponte P. Bucci, Cubo 33C, 87036 Rende, Cosenza, Italy

² CNR-Nanotec, via Ponte P. Bucci, Cubo 33C, 87036 Rende, Cosenza, Italy

³ Department of Physics, Case Western Reserve University, 10600 Euclid Avenue, Cleveland, OH 44106, USA

* Correspondence: giovanna.palermo@unical.it

† These authors contributed equally to this work.

Abstract: Sensitivity and specificity in biosensing platforms remain key aspects to enable an effective technological transfer. Considerable efforts have been made to design sensing platforms capable of controlling light–matter interaction at the nanoscale. Here, we numerically investigated how a 3D out-of-plane chiral plasmonic metasurface can be used as a key element in a sensing platform, by exploiting the variation in the plasmonic and lattice modes as a function of the refractive index of the surrounding medium. The results indicate that chiral metasurfaces can be used to perform sensing, by detecting the refractive index change with a maximum sensitivity of 761 nm/RIU. The metasurface properties can be suitably designed to maximize the optical response in terms of the shift, modulated by the refractive index of the analyte molecules. Such studies can pave the way for engineering and fabricating highly selective and specific chiral metasurface-based refractive index sensing platforms.



Citation: Guglielmelli, A.; Nicoletta, G.; Valente, L.; Palermo, G.; Strangi, G. Numerical Modeling of 3D Chiral Metasurfaces for Sensing Applications. *Crystals* **2022**, *12*, 1804. <https://doi.org/10.3390/cryst12121804>

Academic Editor: Jan Macutkevicius

Received: 5 December 2022

Accepted: 9 December 2022

Published: 12 December 2022

Publisher's Note: MDPI stays neutral with regard to jurisdictional claims in published maps and institutional affiliations.



Copyright: © 2022 by the authors. Licensee MDPI, Basel, Switzerland. This article is an open access article distributed under the terms and conditions of the Creative Commons Attribution (CC BY) license (<https://creativecommons.org/licenses/by/4.0/>).

Keywords: metasurface; plasmonics; sensing; refractive index; numerical analysis

1. Introduction

One of the most relevant challenges in the biomedical, environmental, and chemical fields is the biorecognition of analytes in the surrounding environment with high sensitivity and specificity. One possible solution to achieve this goal is to probe the change in the refractive index correlated with the specific molecule or biomolecule that needs to be recognized within a fluid. In this framework, a refractive index sensor, although representing an indirect method, is highly fundamental for biomarker screening, as for example, cancer progression significantly alters the refractive index of cells and tissues [1–3]. With optical sensors, it is possible to retrieve the refractive index in the analyte by converting it into a detectable optical signal. In this direction, the most widely studied is the plasmonic refractive index sensor based on metal nanostructures [4,5]. Optical sensors overcome many limitations of conventional analytical techniques by offering a plethora of advantages: (i) high sensitivity/selectivity, (ii) real-time analyses, (iii) label-free detection of biochemical molecules, and (iv) small sizes [6]. Among them, Surface Plasmon Polaritons (SPP) and Localized Surface Plasmon Resonance (LSPR) sensing are well-established methods based on the shift in the LSPR frequency caused by the change in the refractive index of the nanostructure surrounding medium [7,8]. Through the integration of metasurface, a whole new paradigm shift in sensor technology has been opened up, reaching boosted sensitivity, enhanced detection accuracy, and an even more compact size, easily implementable with lab-on-chip devices [9,10]. Metasurfaces are two-dimensional materials with tailoring subwavelength structures and intriguing optical properties. Each elementary unit of the metasurface, called a meta-atom, is characterized by electromagnetic

resonances very sensitive to changes in the surrounding medium (the analyte layers), hence, appropriate for optical sensors. The resonant electromagnetic spectrum, dominated by the environment, can be suitably tuned by engineering the individual meta-atom's geometry or their periodic arrangements. Different geometries and structural arrangements have been tested to optimize the performance of LSPR sensors, including gold nanocheckerboard arrays [11], gold mushroom arrays [12], gold–silver alloy nanodisk arrays [13], nanopin-cavity resonators [14], gold–silver alloy nanodisks [13], and split-ring resonators [15]. The shifts occurring in the resonant modes of the output spectrum allow the probing of the refractive index of the surrounding molecular analytes. Metasurface-based refractive index sensing platforms present several advantages over conventional SPP-based sensors in terms of fabrication tolerance, reliable readout signal [16], lower radiative damping, and higher quality factors. Moreover, some interesting optical phenomena can occur, such as plasmonically induced transparency [17], Fano resonances [18], multiple resonances, and broadband slow light effects resulting from a complex arrangement of meta-atoms in a unit- or super-cell [19]. In addition, the detection of the small molecules' concentration is allowed due to the confinement of the optical energy into volumes substantially smaller than diffraction-limited optical spots [20]. Furthermore, the sensitive detection of small volumes can be realized by Surface-Enhanced Raman Spectroscopy (SERS) mediated by an inverted pyramidal metasurface [21]. A further step forward in the field of optical sensing has been marked by the advent of chiral metasurfaces, composed of meta-atoms that do not exhibit mirror symmetry. Researchers have been intensively studying chiral metasurfaces for their distinctive chiroptical properties when interacting with either Left- or Right-Circular Polarized light (LCP or RCP). Different chiral structures have been investigated, such as L-shaped [22], twisted Z-shaped [23], dagger-like [24], Shuriken structure [25], gammadion structure [26], diatomic metamolecule shapes [27], twisted propeller blade shapes [28], and a 3D helicoidal structure coupled with a hyperbolic metamaterial [29], just to mention a few. Among the various chiral-dependent phenomena, they display the Circular Dichroism (CD) signal that is the different absorption (or transmission) between the two opposite circularly polarized states of light. This mechanism is part of what is called optical activity, the property of chiral systems to respond to LCP or RCP differently [30]. The circularly polarized light shows a peculiar behavior when interacting with chiral metaelements with a helix-like nanostructure. The light traveling along the helix axis with the same handedness as the helices is reflected, whereas the opposite is transmitted, for frequencies that exceed one octave [31,32]. Due to the fine control of the local fields, the metasurfaces open the possibilities to perform chiral sensing, as theoretically and experimentally demonstrated [26,33]. The interaction of an optically active system with light can be controlled locally, and this has generated enormous interest in achieving metamaterial designs with enhanced chiroptical signals [34]. The design of these sensing platforms is also aimed to improve the chiroptical signals of different biomolecules with Ultraviolet (UV), visible, and Infrared (IR) CD bands [35–37].

In our work, we designed a metasurface consisting of 3D chiral gold helices periodically arranged in a 2D square lattice. We systematically investigated the influence of the structural parameters (number of helix pitch— N , dimension on the unit cell— a , and angle of incidence— θ) on the resonant peaks. Furthermore, to test the metasurface performance in terms of the refractive index sensor, we performed simulations by changing the surrounding medium refractive index. The estimated sensing sensitivity and the Figure Of Merit FOM values were in the range of 450–761 nm/RIU and 9.9–12.3 RIU^{−1}, respectively. In addition, by taking advantage of the structure chirality, we analyzed the polarization sensitivity (or the CD signal) of the structure to the incident light by changing its polarization state, proposing also a molecular detection exploiting the CD signal. The obtained results for the design of such compact chiral plasmonic metasurface can open different possibilities to achieve multifunctionality, such as optical absorption, circular dichroism, and highly sensitive refractive index sensing.

2. Materials and Methods

The modeled metasurface was based on 3D out-of-plane gold helices periodically arranged in a 2D square lattice. It has been reported that COMSOL Multiphysics can numerically solve phenomena, such as electromagnetic wave propagation and light–matter interactions, that are mathematically described using Partial Differential Equations (PDEs) and are comparable with experimental results [38–41].

In this work, the simulations were carried out using the COMSOL Multiphysics module for the Electromagnetic Waves, Frequency Domain (EWFDM). To solve electromagnetic equations, COMSOL uses the Finite Element Method (FEM). Maxwell’s equations in three dimensions are simplified by considering that fields vary sinusoidally in time at a known angular frequency and that all material properties are linear concerning field strength [42]:

$$\nabla \times (\mu_r^{-1} \nabla \times \mathbf{E}) - \left(\frac{\omega^2}{c_0^2} \right) \epsilon_r - \left(\frac{i\sigma}{\omega\epsilon_0} \right) \mathbf{E} = 0, \quad (1)$$

where μ_r , ϵ_r , and σ are the relative permeability, the relative permittivity, and the electrical conductivity related to the materials, respectively. The equation is solved for $\mathbf{E} = E(x, y, z)$ from which the other physical quantities can be obtained. The COMSOL module offered the possibility to choose the electric displacement field model: the refractive index was the default option used. It was possible to set the real and imaginary parts of the refractive index, called n and k , and the relative permittivity:

$$\epsilon_r = (n - ik)^2. \quad (2)$$

To simulate the metasurface, we chose a 3D geometry consisting of a parallelepiped with the height six times the unit cell dimension a , where a must be comparable with the incident wavelength. Each single block consisted of three main parts, starting from the bottom: (a) the glass with a refractive index $n_{glass} = 1.5$; (b) the single right-handed gold helix (Johnson and Christy refractive index), and (c) the surrounding medium with a variable refractive index n_{medium} . To create a wave diffusion environment, an input (*Port1*) and an output port (*Port2*) were used, respectively, one on the top for the emitted radiation and the other on the bottom for the detection. To ensure the infinity conditions in the (x, y) plane, the Periodic Boundary Conditions (PBCs) were applied to the surfaces along the (x, y) directions of the blocks. To simulate the repeated single unit cell, the Floquet periodicity was used, which is useful in frequency domain problems. In addition to the PBCs, Perfect Matched Layers (PMLs) were introduced into the simulated system, to reproduce an absorbing boundary condition at the block extremes. The equations were solved by discretizing the problem, creating a dense mesh with control over the single components of the constructed geometry. In particular, for this work, an “extra-fine” mesh was chosen that consisted of free triangular and tetrahedral geometry with 82,717 domain, 8024 boundary, and 710 edge elements. The ideal mesh should preferably have the smallest component dimension of approximately one-half wavelength of the wave.

The polarization (linear, circular, and elliptical) and the incident angle of the impinging radiation can be suitably selected [43], depending on the particular optical property to be investigated. In the first part of the numerical analysis, a Transverse Magnetic (TM) polarization out of plane was used, with the magnetic field amplitude:

$$\mathbf{H}_0 = \begin{pmatrix} 0 \\ 1 \\ 0 \end{pmatrix}. \quad (3)$$

In the second part of the numerical investigation, Left- and Right-Circular Polarized (LCP and RCP) light were propagated by setting the following amplitude:

$$\mathbf{E}_0 = \begin{pmatrix} 1 \\ -1i \\ 0 \end{pmatrix}, \mathbf{E}_0 = \begin{pmatrix} 1 \\ 1i \\ 0 \end{pmatrix}. \quad (4)$$

The top port boundary condition propagated a plane wave at the specified incident angle θ and computed the reflected light, while the bottom one calculated the transmitted light. Through the coefficient of the Scattering Matrix S , it was possible to evaluate different optical parameters, such as the Reflectance (R), Transmittance (T), and Absorption (A) of the modeled structure. In particular, (i) the S_{11} parameter provided information regarding the amount of light reflected compared to that sent from the input *Port1*, while (ii) the S_{21} parameter quantified how much of the transmitted light reached the output *Port2* [29]. The equations for the two parameters are shown below:

$$S_{11} = \frac{\int_{port1} ((\mathbf{E}_C - \mathbf{E}_1) \cdot \mathbf{E}_1^*) dA_1}{\int_{port1} (\mathbf{E}_1 \cdot \mathbf{E}_1^*) dA_1}, \quad (5)$$

$$S_{21} = \frac{\int_{port2} ((\mathbf{E}_C - \mathbf{E}_2) \cdot \mathbf{E}_2^*) dA_2}{\int_{port2} (\mathbf{E}_2 \cdot \mathbf{E}_2^*) dA_2}, \quad (6)$$

where E_C is the computed electric field equal to $E_C = \sum_{i=1} S_{i1} \mathbf{E}_i$. The fields were normalized concerning the integration of the power flow across each port cross section A_1 and A_2 , respectively. The absorbance was easily derived by knowing the other two optical quantities, as $A = 1 - (T + R)$.

3. Results and Discussion

Figure 1a shows the single structure analyzed, where the physical dimensions are reported: a is the dimension of the unit cell, r is the wire radius (16 nm), R is the helix radius (25 nm), p is the axial pitch (60 nm) that represents the spatial distance between two turns of the helix, N is the number of pitches, and θ is the angle of incidence for the helix axis. Some of these parameters were varied to investigate the influence on the resonances number and sharpness and to find the optimal conditions for highly effective refractive index sensing; in particular, the periodicity in plane (a) and the periodicity out of plane (N) were varied. In Figure 1b,c the resulting right-handed helical arrays for two values of a , $a = 100$ nm and $a = 250$ nm, are shown, respectively.

In Figure 2a–c, the normalized absorbance maps are shown as a function of three different parameters a , N , and θ in the wavelength range (400–1300) nm. In particular, the tested values for a were 100, 150, 200, and 250 nm; for N , they were 1, 2, 3, and 4, while for θ , they were 40, 50, and 60°. Following the results obtained by varying the first parameter a (see Figure 2a), we chose 250 nm as the in-plane periodicity of the helix array to guarantee three distinct, intense, and narrow resonances in the wavelength range between 750 and 1300 nm. Although the most intense absorption band was found in the range between 400 and 600 nm, this region was excluded from the other analyses because it was not of interest for two reasons: (i) the spectral band was broad and so not ideal for sensing, (ii) the visible region is where most biomolecules absorb, so it can also affect the analyte properties and create signal overlapping. After the in-plane periodicity a was fixed, the influence of the out-of-plane periodicity N was evaluated. From this analysis (see Figure 2b), it emerged that the most intense modes, in the same range of wavelengths evaluated before, were found for N equal to 3. This value was also perfectly suited to the purpose of detecting the refractive index of a surrounding medium, as it allowed a sufficiently large and extensive out-of-plane sensing surface [29]. Ultimately, the effect of the incident angle θ was investigated (see Figure 2c), discovering that the value that ensured the best performance in terms of absorption, in the range 750–1300 nm, was 50°. It can be noticed that even an incident angle of 60° could be taken into consideration, as it provided intense resonances, but the best compromise between the intensity and width of the resonances in the range 750–1300 nm was guaranteed by $\theta = 50^\circ$.

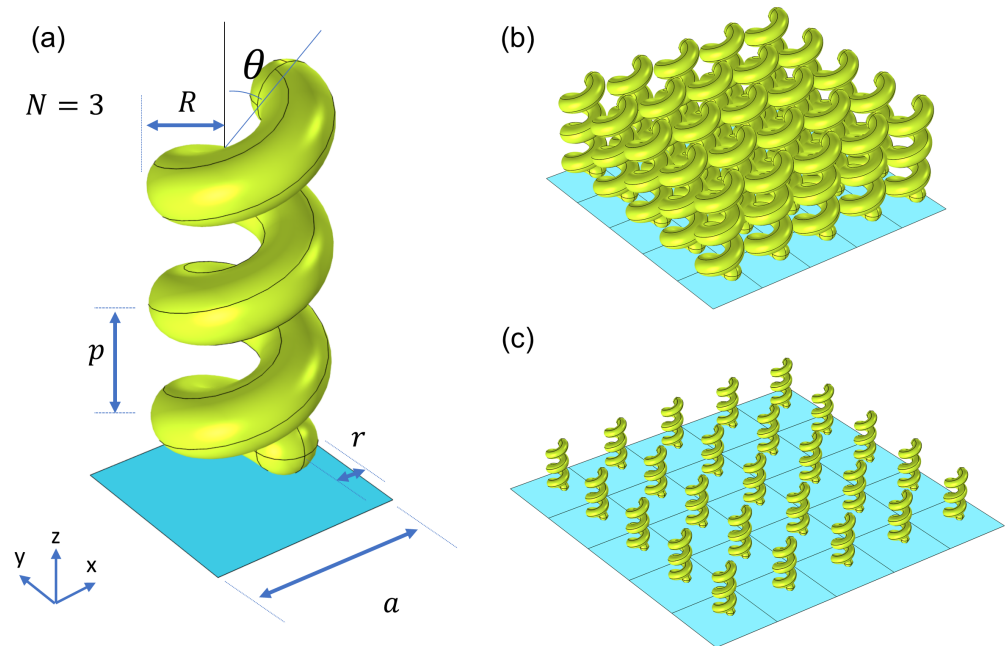


Figure 1. (a) The geometry of one lateral unit cell of the out-of-plane chiral structure composed of a right-handed Au helix on a glass substrate with the relevant structure parameters illustrated: the wire radius (r), helix radius (R), axial pitch (p), and the lattice constant (a). The out-of-plane periodicity is indicated by N . The geometry of the chiral metasurface for (b) $a = 100$ nm and (c) $a = 250$ nm.

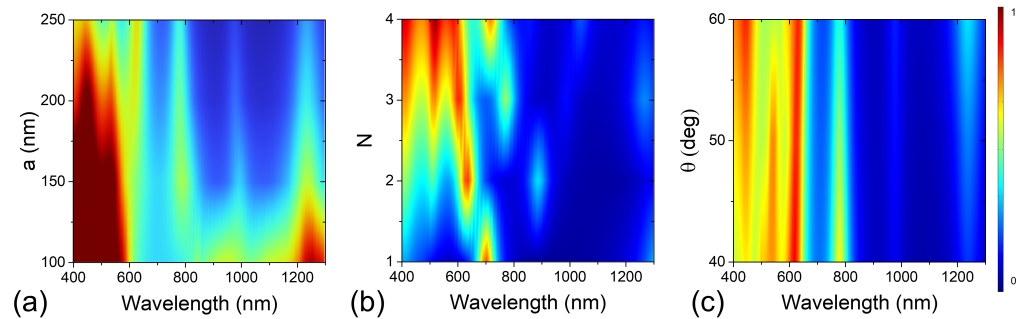


Figure 2. Normalized absorbance map of the plasmonic metasurface as a function of (a) the in-plane periodicity a in the range 100–250 nm and (b) the out-of-plane periodicity N in the range 1–4. (c) The angle of incidence in the range 40–60°.

To test the capability of the tailored plasmonic metasurface as a highly sensitive refractive index sensor, the 1,2,3-Propantriol (glycerol) molecule was selected as a model analyte to be detected. Different percentage concentrations of glycerol dissolved in an aqueous solution were tested (2.1, 8.5, 17.5, 38.2, 59.0, 69.2, and 82.4%), corresponding to as many different refractive indices (1.345, 1.375, 1.401, 1.437, 1.455, 1.461, and 1.467) [44]. The spectral shift interrogation in terms of wavelength change represented the easiest and most reliable way to perform refractive index sensing compared with intensity interrogation. This is related to the influence of the surrounding media on the resonance condition that reflects it in the spectral shifts, more specifically on the dielectric permittivity [22]. To this end, the parameters carefully chosen by conducting the first parametric analysis ($a = 250$ nm, $N = 3$, and $\theta = 50^\circ$), made it possible to obtain a spectrum with three narrow and intense absorption lines in the infrared spectral range. Indeed, the tailored configuration of the periodic structure offered better spectral response with multiple resonant peaks in particular

at 792, 957, and 1173 nm, as shown in Figure 3a, allowing cross-checking and comparing the wavelength interrogation with multiple peaks with more reliable results.

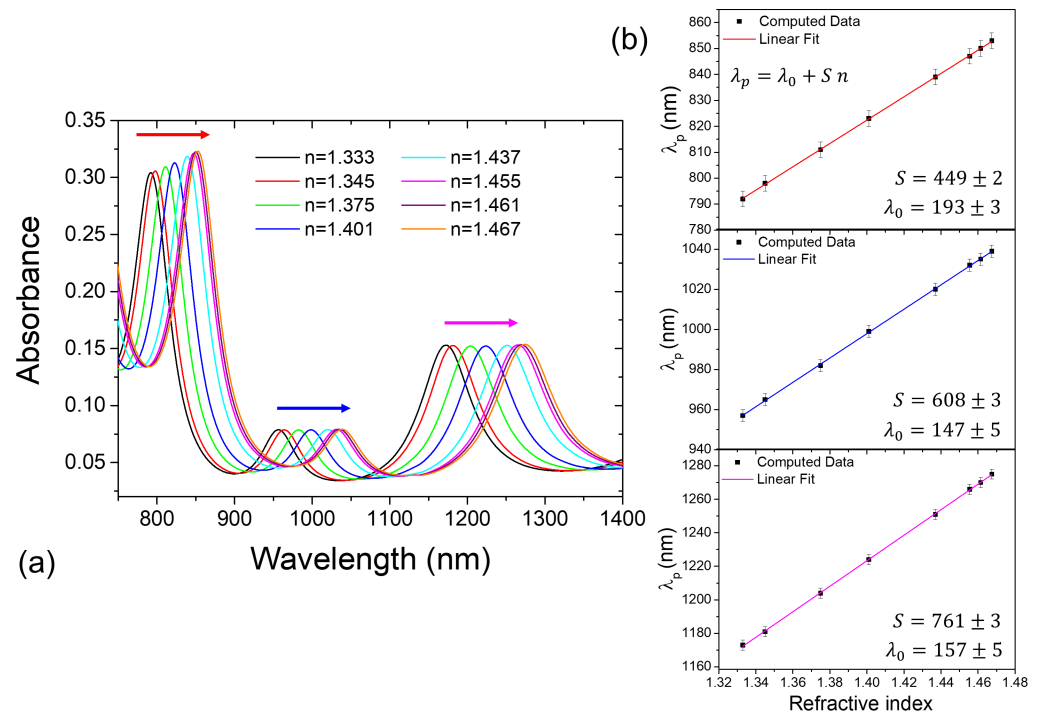


Figure 3. (a) Spectral characterization of the plasmonic metasurface: absorbance spectra calculated for different concentrations of 1,2,3-Propantriol for $a = 250$ nm; (b) linear fit of the peak wavelength plotted versus the refractive index of the medium for the three resonant modes. The fitting equation is $\lambda_p = \lambda_0 + Sn$; the correlation coefficient is $R = 0.99$ for the three fits.

In Figure 3a, the three arrows indicate the gradual red shift of the resonant peaks registered by constantly increasing the refractive index from 1.333 (water) to 1.467 (82.4% glycerol), while in Figure 3b, the corresponding peak positions as a function of the refractive index, are reported. The three plots (see Figure 3b, top, middle, and bottom panels) highlight the linear behavior between λ_p and n (the black squares are the computed data points, and the straight lines are the linear fits). For sensing applications, a linear change in the λ_p is usually preferable for refractive index sensing of a given unknown medium [22]. From the slope of the fitting equation $\lambda_p = \lambda_0 + Sn$, the sensitivity S value for each peak can be retrieved. Alternatively, the formula to derive the spectral sensitivity (nm/RIU) is $S = \Delta n / \Delta \lambda$, where Δn is the change in the refractive index, and $\Delta \lambda$ is the resonance peak shift. The extracted S values were found to be in the 449–761 nm/RIU range. As can be seen from the reported results in Figure 3b, the peak at 1173 nm was the one that mainly underwent the red shift as the refractive index increased, resulting in a sensitivity value of 761 nm/RIU. It is worth noting that this mode, which was most affected by in-plane periodicity, was therefore dependent on the inter-structure interaction, as can be seen from the absorption map in Figure 2a. By calculating the Full Width at Half Maximum ($FWHM$), another sensing-related parameter was deduced, the figure of merit ($FOM = S / FWHM$). The resulting $FOMs$, for the three resonant peaks were in the range 9.9–12.3 RIU⁻¹, by taking into account the average $FWHM$ values. The calculated values were comparable with the value range reported in other works [24,45,46] that used metasurfaces with different geometries, L-shaped, U-shaped, and spiral G-shaped. In Figure 4, it is possible to see the distribution of the electric field enhancement ($|E| / E_0$) on the helix surface at the three resonance peaks. A significant enhancement of the electric field can be appreciated for the absorbance peak at 792 nm (≈ 9), at 957 nm (≈ 6), and 1173 nm (≈ 6).

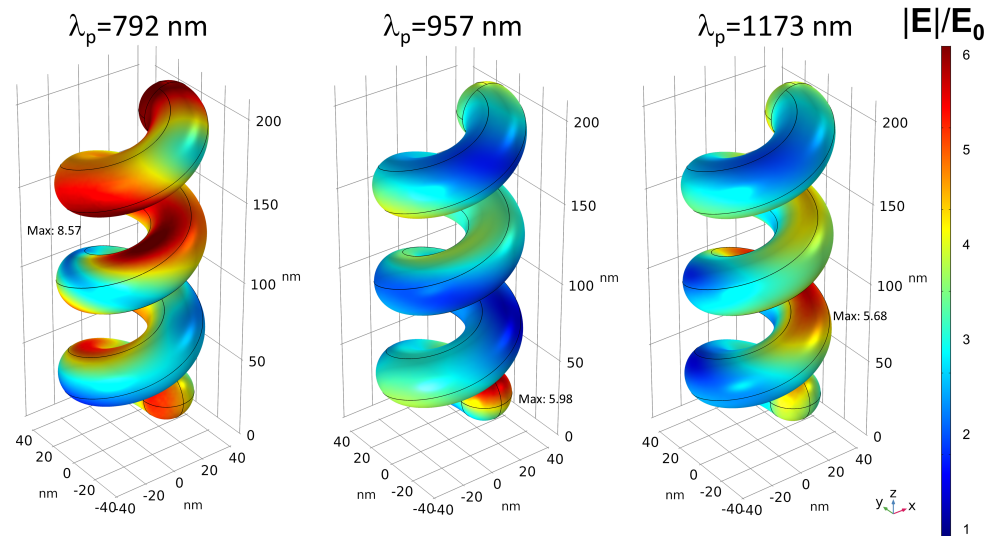


Figure 4. Electric field enhancement on the helix surface at the three λ_p : 792 nm, 957 nm, and 1173 nm.

The intrinsic chiral nature of the plasmonic metasurface considered allowed using dichroic signals for sensing applications. In this case, it was possible to exploit the absence of the intrinsic mirror symmetry of the structure and the corresponding difference in its interaction with circularly polarized light. For this reason, the same numerical model was modified to have both Left-handed Circular Polarized (LCP) and Right-handed Circular Polarized (RCP) light affecting the structure, with an incidence angle equal to 50° . In the Materials and Methods section, we described how it was possible to propagate Circular Polarized waves in Comsol Multiphysics. In Figure 5a,b, it is possible to see the absorbance and transmittance curves for the plasmonic metasurface characterized by an in-plane periodicity $a = 250$ nm, considering only water as the surrounding medium. It is possible to observe a greater coupling between the right-handed structure and the RCP light, which led to more peaked absorbance modes than those obtained in the case of the LCP wave, indicative of a better coupling between the light and the metasurface. In Figure 5c, we report the Circular Dichroism (CD) that was calculated using the relations, $CD_{Abs} = A_{LCP} - A_{RCP}$, in the absorption mode, by varying the refractive index of the medium surrounding the helices, for values corresponding to 38% and 82% glycerol in water.

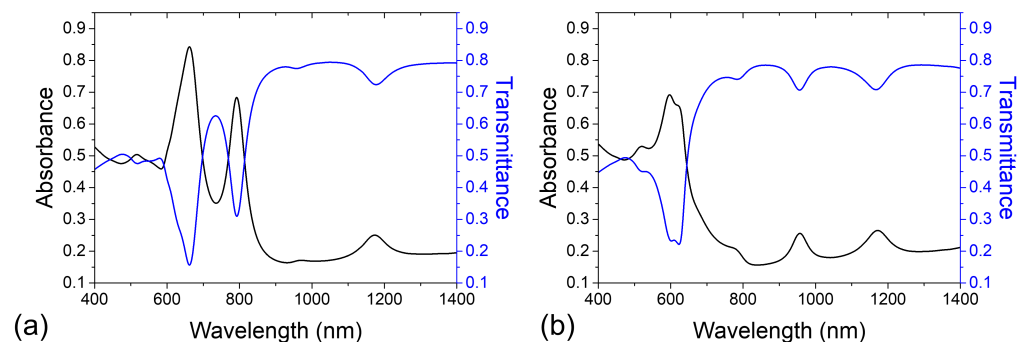


Figure 5. Cont.

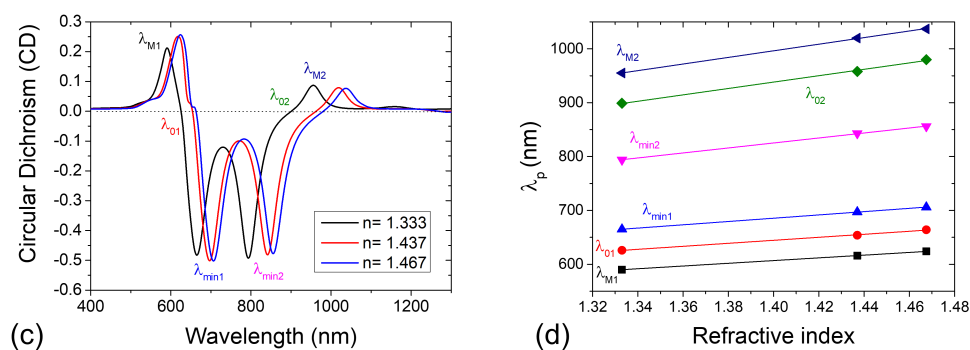


Figure 5. Absorbance and transmittance spectra of the plasmonic metasurface for (a) Right-Circular Polarized (RCP) and (b) Left-Circular Polarized (LCP) light. (c) CD spectra calculated in a 1,2,3-Propantriol–water solution at different molar concentrations ranging from 0% (corresponding to water ($n = 1.333$)) to 82% 1,2,3-Propantriol in water ($n = 1.467$). (d) Linear fit of the peak wavelength plotted versus the refractive index of the medium.

From the figure, several CD features can be identified corresponding to maxima ($\lambda_{M1} = 590$ nm, $\lambda_{M2} = 955$ nm), minima ($\lambda_{min1} = 665$ nm, $\lambda_{min2} = 794$ nm), and zero dichroism points ($\lambda_{01} = 626$ nm, $\lambda_{02} = 899$ nm). Following the index variation, there was a shift of the modes from which it was possible to determine the bulk refractive index sensitivity S of the structure. In particular, we found S in the range 252–614 nm/RIU with an FOM in the range 6–11 RIU^{−1}. The proposed chiral plasmonic metasurface based on 3D gold helices may find specific application as a refractive index sensor for detecting different molecules, due to the high sensitivity achieved in the sensing performance.

4. Conclusions

In conclusion, a multipurpose chiral plasmonic metasurface that consisted of an array of 3D right-handed gold helices was proposed and numerically explored. To investigate the influence of different geometrical parameters on the multiple resonant modes supported by the structure, a systematic parametric analysis was performed. We found the optimal combination of parameters to design a metasurface ($a = 250$ nm, $N = 3$, and $\theta = 50^\circ$) to achieve appropriate distinct resonance modes in the IR region ideal for refractive index sensing. The IR modes allowed performing a minimally invasive refractive index biosensing, compared to UV–visible modes that overlap with absorption bands of different biomolecules. The sensing performances were tested by simulating different concentrations of glycerol as the surrounding medium. The calculated sensing sensitivity and the FOM values in the range of 450–761 nm/RIU and 9.9–12.3 RIU^{−1}, respectively, suggest that the tailored metasurface can be employed for surface sensing. In addition, the designed metasurface showed highly chiral behavior with tunable multiband CD covering a wide spectral range from 400 to 1300 nm. The interesting optical properties observed for this 3D chiral plasmonic metasurface can pave the way for the ad hoc design of a highly sensitive surface integrable in multifunctional compact chips for optical absorption, circular dichroism, and refractive index sensing.

Author Contributions: A.G. and G.N. contributed equally to this work. Investigation, A.G. and G.N.; data curation, L.V.; Conceptualization, review and editing, G.P. and A.G.; supervision, G.S. The manuscript was written through the contributions of all authors. All authors have given approval to the final version of the manuscript.

Funding: G.P. acknowledges the financial support from “AIM: Attraction and International Mobility”—PON R&I 2014–2020 Calabria. G.N. acknowledges the financial support from “Dottorati innovativi a caratterizzazione industriale”—PON R&I FSE-FESR 2014–2020. A.G. acknowledges the financial support from the “NLHT- Nanoscience Laboratory for Human Technologies”—(POR Calabria FESR-FSE 14/20).

Data Availability Statement: The data that support the findings of this study are available within the article.

Conflicts of Interest: The authors declare no conflict of interest.

Abbreviations

The following abbreviations are used in this manuscript:

| | |
|------|---|
| SPP | Surface Plasmon Polaritons |
| LSPR | Localized Surface Plasmon Resonances |
| SERS | Surface Enhanced Raman Spectroscopy |
| LCP | Left Circular Polarized |
| RCP | Right Circular Polarized |
| CD | Circular Dichroism |
| UV | Ultraviolet |
| IR | Infrared |
| FOM | Figure of Merit |
| EWFD | Electromagnetic Waves, Frequency Domain |
| PDEs | Partial Differential Equations |
| FEM | Finite Element Method |
| PBCs | Periodic Boundary Conditions |
| PMLs | Perfect Matched Layers |
| TM | Transverse Magnetic |
| R | Reflectance |
| T | Transmittance |
| A | Absorbance |
| FWHM | Full Width at Half Maximum |
| E | Electric Field |
| RIU | Refractive Index Unit |

References

- Lin, X.; Wan, N.; Weng, L.; Zhou, Y. Light scattering from normal and cervical cancer cells. *Appl. Opt.* **2017**, *56*, 3608–3614. [[CrossRef](#)] [[PubMed](#)]
- Wang, Z.; Popescu, G.; Tangella, K.V.; Balla, A. Tissue refractive index as marker of disease. *J. Biomed. Opt.* **2011**, *16*, 116017. [[CrossRef](#)] [[PubMed](#)]
- Ekpenyong, A.E.; Man, S.M.; Achouri, S.; Bryant, C.E.; Guck, J.; Chalut, K.J. Bacterial infection of macrophages induces decrease in refractive index. *J. Biophotonics* **2013**, *6*, 393–397. [[CrossRef](#)] [[PubMed](#)]
- Chau, Y.F.C.; Wang, C.K.; Shen, L.; Lim, C.M.; Chiang, H.P.; Chao, C.T.C.; Huang, H.J.; Lin, C.T.; Kumara, N.; Voo, N.Y. Simultaneous realization of high sensing sensitivity and tunability in plasmonic nanostructures arrays. *Sci. Rep.* **2017**, *7*, 16817. [[CrossRef](#)] [[PubMed](#)]
- Špačková, B.; Wrobel, P.; Bocková, M.; Homola, J. Optical biosensors based on plasmonic nanostructures: A review. *Proc. IEEE* **2016**, *104*, 2380–2408. [[CrossRef](#)]
- Khan, S.A.; Khan, N.Z.; Xie, Y.; Abbas, M.T.; Rauf, M.; Mehmood, I.; Runowski, M.; Agathopoulos, S.; Zhu, J. Optical sensing by metamaterials and metasurfaces: From physics to biomolecule detection. *Adv. Opt. Mater.* **2022**, *10*, 2200500. [[CrossRef](#)]
- Yavas, O.; Acimovic, S.S.; Garcia-Guirado, J.; Berthelot, J.; Dobosz, P.; Sanz, V.; Quidant, R. Self-calibrating on-chip localized surface plasmon resonance sensing for quantitative and multiplexed detection of cancer markers in human serum. *ACS Sens.* **2018**, *3*, 1376–1384. [[CrossRef](#)]
- Martinsson, E.; Shahjamali, M.M.; Enander, K.; Boey, F.; Xue, C.; Aili, D.; Liedberg, B. Local refractive index sensing based on edge gold-coated silver nanoprisms. *J. Phys. Chem. C* **2013**, *117*, 23148–23154. [[CrossRef](#)]
- Tseng, M.L.; Jahani, Y.; Leitis, A.; Altug, H. Dielectric metasurfaces enabling advanced optical biosensors. *ACS Photonics* **2020**, *8*, 47–60. [[CrossRef](#)]
- Bouchal, P.; Dvorak, P.; Babocký, J.; Bouchal, Z.; Ligmajer, F.; Hrtón, M.; Krapek, V.; Faßbender, A.; Linden, S.; Chmelík, R.; et al. High-resolution quantitative phase imaging of plasmonic metasurfaces with sensitivity down to a single nanoantenna. *Nano Lett.* **2019**, *19*, 1242–1250. [[CrossRef](#)]
- Cai, J.; Zhang, C.; Liang, C.; Min, S.; Cheng, X.; Li, W.D. Solution-Processed Large-Area Gold Nanocheckerboard Metasurfaces on Flexible Plastics for Plasmonic Biomolecular Sensing. *Adv. Opt. Mater.* **2019**, *7*, 1900516. [[CrossRef](#)]
- Shen, Y.; Zhou, J.; Liu, T.; Tao, Y.; Jiang, R.; Liu, M.; Xiao, G.; Zhu, J.; Zhou, Z.K.; Wang, X.; et al. Plasmonic gold mushroom arrays with refractive index sensing figures of merit approaching the theoretical limit. *Nat. Commun.* **2013**, *4*, 2381. [[CrossRef](#)] [[PubMed](#)]

13. Misbah, I.; Zhao, F.; Shih, W.C. Symmetry breaking-induced plasmonic mode splitting in coupled gold–silver alloy nanodisk array for ultrasensitive RGB colorimetric biosensing. *ACS Appl. Mater. Interfaces* **2018**, *11*, 2273–2281. [[CrossRef](#)] [[PubMed](#)]
14. Fan, J.R.; Zhu, J.; Wu, W.G.; Huang, Y. Plasmonic Metasurfaces Based on Nanopin-Cavity Resonator for Quantitative Colorimetric Ricin Sensing. *Small* **2017**, *13*, 1601710. [[CrossRef](#)]
15. Patel, S.K.; Surve, J.; Katkar, V.; Parmar, J.; Al-Zahrani, F.A.; Ahmed, K.; Bui, F.M. Encoding and tuning of THz metasurface-based refractive index sensor with behavior prediction using XGBoost Regressor. *IEEE Access* **2022**, *10*, 24797–24814. [[CrossRef](#)]
16. Lee, Y.; Kim, S.J.; Park, H.; Lee, B. Metamaterials and metasurfaces for sensor applications. *Sensors* **2017**, *17*, 1726. [[CrossRef](#)]
17. Liu, N.; Weiss, T.; Mesch, M.; Langguth, L.; Eigenthaler, U.; Hirscher, M.; Sonnichsen, C.; Giessen, H. Planar metamaterial analogue of electromagnetically induced transparency for plasmonic sensing. *Nano Lett.* **2010**, *10*, 1103–1107. [[CrossRef](#)]
18. Khanikaev, A.B.; Wu, C.; Shvets, G. Fano-resonant metamaterials and their applications. *Nanophotonics* **2013**, *2*, 247–264. [[CrossRef](#)]
19. Wu, C.; Khanikaev, A.B.; Shvets, G. Broadband slow light metamaterial based on a double-continuum Fano resonance. *Phys. Rev. Lett.* **2011**, *106*, 107403. [[CrossRef](#)]
20. Li, Z.; Zhu, Y.; Hao, Y.; Gao, M.; Lu, M.; Stein, A.; Park, A.H.A.; Hone, J.C.; Lin, Q.; Yu, N. Hybrid metasurface-based mid-infrared biosensor for simultaneous quantification and identification of monolayer protein. *ACS Photonics* **2019**, *6*, 501–509. [[CrossRef](#)]
21. Palermo, G.; Rippa, M.; Conti, Y.; Vestri, A.; Castagna, R.; Fusco, G.; Suffredini, E.; Zhou, J.; Zyss, J.; De Luca, A.; et al. Plasmonic metasurfaces based on pyramidal nanoholes for high-efficiency SERS biosensing. *ACS Appl. Mater. Interfaces* **2021**, *13*, 43715–43725. [[CrossRef](#)] [[PubMed](#)]
22. Mandal, P. Highly Absorptive Chiral L-Shape MDM plasmonic metasurface as multifunction device: Design and computational studies. *Plasmonics* **2021**, *16*, 1391–1403. [[CrossRef](#)]
23. Qu, Y.; Huang, L.; Wang, L.; Zhang, Z. Giant circular dichroism induced by tunable resonance in twisted Z-shaped nanostructure. *Opt. Express* **2017**, *25*, 5480–5487. [[CrossRef](#)] [[PubMed](#)]
24. Mandal, P. Au–Al multi-metal bilayer dagger-like structure for broadband circular dichroism and tunability. *Optik* **2020**, *204*, 164222. [[CrossRef](#)]
25. Kelly, C.; Tullius, R.; Laphorn, A.J.; Gadegaard, N.; Cooke, G.; Barron, L.D.; Karimullah, A.S.; Rotello, V.M.; Kadodwala, M. Chiral plasmonic fields probe structural order of biointerfaces. *J. Am. Chem. Soc.* **2018**, *140*, 8509–8517. [[CrossRef](#)]
26. Hendry, E.; Carpy, T.; Johnston, J.; Popland, M.; Mikhaylovskiy, R.; Laphorn, A.; Kelly, S.; Barron, L.; Gadegaard, N.; Kadodwala, M. Ultrasensitive detection and characterization of biomolecules using superchiral fields. *Nat. Nanotechnol.* **2010**, *5*, 783–787. [[CrossRef](#)]
27. Liang, Y.; Lin, H.; Koshelev, K.; Zhang, F.; Yang, Y.; Wu, J.; Kivshar, Y.; Jia, B. Full-stokes polarization perfect absorption with diatomic metasurfaces. *Nano Lett.* **2021**, *21*, 1090–1095. [[CrossRef](#)]
28. Ji, C.Y.; Chen, S.; Han, Y.; Liu, X.; Liu, J.; Li, J.; Yao, Y. Artificial Propeller Chirality and Counterintuitive Reversal of Circular Dichroism in Twisted Meta-molecules. *Nano Lett.* **2021**, *21*, 6828–6834. [[CrossRef](#)]
29. Palermo, G.; Lio, G.E.; Esposito, M.; Ricciardi, L.; Manoccio, M.; Tasco, V.; Passaseo, A.; De Luca, A.; Strangi, G. Biomolecular sensing at the interface between chiral metasurfaces and hyperbolic metamaterials. *ACS Appl. Mater. Interfaces* **2020**, *12*, 30181–30188. [[CrossRef](#)]
30. Zhu, A.Y.; Chen, W.T.; Zaidi, A.; Huang, Y.W.; Khorasaninejad, M.; Sanjeev, V.; Qiu, C.W.; Capasso, F. Giant intrinsic chiro-optical activity in planar dielectric nanostructures. *Light. Sci. Appl.* **2018**, *7*, 17158–17158. [[CrossRef](#)]
31. Gansel, J.K.; Thiel, M.; Rill, M.S.; Decker, M.; Bade, K.; Saile, V.; von Freymann, G.; Linden, S.; Wegener, M. Gold helix photonic metamaterial as broadband circular polarizer. *Science* **2009**, *325*, 1513–1515. [[CrossRef](#)] [[PubMed](#)]
32. Gansel, J.K.; Wegener, M.; Burger, S.; Linden, S. Gold helix photonic metamaterials: A numerical parameter study. *Opt. Express* **2010**, *18*, 1059–1069. [[CrossRef](#)] [[PubMed](#)]
33. Tang, Y.; Cohen, A.E. Optical chirality and its interaction with matter. *Phys. Rev. Lett.* **2010**, *104*, 163901. [[CrossRef](#)] [[PubMed](#)]
34. Yoo, S.; Park, Q.H. Metamaterials and chiral sensing: A review of fundamentals and applications. *Nanophotonics* **2019**, *8*, 249–261. [[CrossRef](#)]
35. Zhao, Y.; Askarpour, A.N.; Sun, L.; Shi, J.; Li, X.; Alù, A. Chirality detection of enantiomers using twisted optical metamaterials. *Nat. Commun.* **2017**, *8*, 14180. [[CrossRef](#)] [[PubMed](#)]
36. Hentschel, M.; Schäferling, M.; Duan, X.; Giessen, H.; Liu, N. Chiral plasmonics. *Sci. Adv.* **2017**, *3*, e1602735. [[CrossRef](#)] [[PubMed](#)]
37. García-Guirado, J.; Svedendahl, M.; Puigdollers, J.; Quidant, R. Enantiomer-selective molecular sensing using racemic nanoplasmonic arrays. *Nano Lett.* **2018**, *18*, 6279–6285. [[CrossRef](#)]
38. Multiphysics, C. *Introduction to Comsol Multiphysics®*; COMSOL Multiphysics: Burlington, MA, USA, 1998; Volume 9, p.32.
39. Dickinson, E.J.; Ekström, H.; Fontes, E. COMSOL Multiphysics®: Finite element software for electrochemical analysis. A mini-review. *Electrochem. Commun.* **2014**, *40*, 71–74. [[CrossRef](#)]
40. Lio, G.E.; Palermo, G.; Caputo, R.; De Luca, A. A comprehensive optical analysis of nanoscale structures: From thin films to asymmetric nanocavities. *RSC Adv.* **2019**, *9*, 21429–21437. [[CrossRef](#)]
41. Palermo, G.; Sreekanth, K.V.; Maccaferri, N.; Lio, G.E.; Nicoletta, G.; De Angelis, F.; Hinczewski, M.; Strangi, G. Hyperbolic dispersion metasurfaces for molecular biosensing. *Nanophotonics* **2021**, *10*, 295–314. [[CrossRef](#)]
42. Lininger, A.; Palermo, G.; Guglielmelli, A.; Nicoletta, G.; Goel, M.; Hinczewski, M.; Strangi, G. Chirality in Light–Matter Interaction. *Adv. Mater* **2022**, 2107325. [[CrossRef](#)] [[PubMed](#)]

43. Lio, G.E.; Palermo, G.; Caputo, R.; De Luca, A. Opto-mechanical control of flexible plasmonic materials. *J. Appl. Phys.* **2019**, *125*, 082533. [[CrossRef](#)]
44. Koohyar, F.; Kiani, F.; Sharifi, S.; Sharifirad, M.; Rahmanpour, S.H. Study on the change of refractive index on mixing, excess molar volume and viscosity deviation for aqueous solution of methanol, ethanol, ethylene glycol, 1-propanol and 1, 2, 3-propantriol at T= 292.15 K and atmospheric pressure. *Res. J. Appl. Sci. Eng. Technol.* **2012**, *4*, 3095–3101.
45. Xu, X.; Peng, B.; Li, D.; Zhang, J.; Wong, L.M.; Zhang, Q.; Wang, S.; Xiong, Q. Flexible visible–infrared metamaterials and their applications in highly sensitive chemical and biological sensing. *Nano Lett.* **2011**, *11*, 3232–3238. [[CrossRef](#)] [[PubMed](#)]
46. Ren, M.; Pan, C.; Li, Q.; Cai, W.; Zhang, X.; Wu, Q.; Fan, S.; Xu, J. Isotropic spiral plasmonic metamaterial for sensing large refractive index change. *Opt. Lett.* **2013**, *38*, 3133–3136. [[CrossRef](#)]